Enhanced Photocatalytic CO$_2$ Reduction by Novel Designed Porphyrin-Based MOFs: From Accurate QSPR Model to Experimental Exploration

Leila Tayebi, Rahmatollah Rahimi,* and Ali Reza Akbarzadeh*

Read Online

ACCESS | Metrics & More | Article Recommendations | SI Supporting Information

ABSTRACT: A reliable quantitative structure−property relationship (QSPR) model was established for predicting the evolution rate of CO$_2$ photoreduction over porphyrin-based metal−organic frameworks (MOFs) as photocatalysts. The determination coefficient (R^2) for both training and test sets was 0.999. The root-mean-squared error of prediction (RMSEP) obtained was 0.006 and 0.005 for training and test sets, respectively. Based on the proposed model, two porphyrin-based MOFs, Cu-PMOF and Co-PMOF, were designed, synthesized, and applied for CO$_2$ photoreduction under UV−visible irradiation without any additional photosensitizer. The X-ray diffraction (XRD), diffuse reflectance spectroscopy (DRS), and Fourier transform infrared (FTIR) measurements revealed the successful formation of the porous MOFs. The N$_2$ adsorption isotherms at 77 K showed a high Brunauer−Emmett−Teller (BET) surface area of 932.64 and 974.06 m^2·g^{-1} for Cu-PMOF and Co-PMOF, respectively. Theoretical and experimental results showed that HCOOH evolution rates over Cu-PMOF and Co-PMOF were (127.80, 101.62 μmol) and (130.6, 103.47 μmol), respectively. These results were robust and satisfactory.
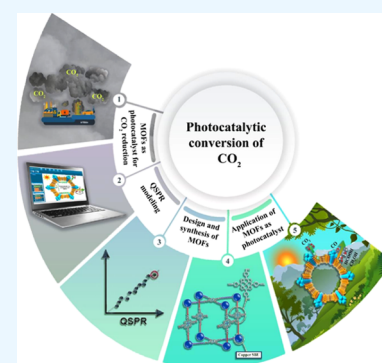
1. INTRODUCTION

In the past few decades, burning fossil fuels has increased significantly due to the intense energy demands. As a result, the primary greenhouse gas (CO$_2$) has become the main factor of global warming and has attracted much attention because of environmental problems.[1] Therefore, one of the best strategies involves developing effective CO$_2$ capture and conversion methods to mitigate carbon dioxide emissions. The photocatalytic conversion of the captured CO$_2$ into value-added chemicals is an effective strategy to utilize CO$_2$, which can directly transform CO$_2$ into useful products such as methanol,[2] methane,[3] carbon monoxide,[4,5] and formic acid.[6,7]

Extensive efforts have been made to explore high-performance photocatalytic systems for CO$_2$ reduction. There are several essential features to construct highly efficient photocatalysts, such as suitable light harvesting, rapid photogeneration of electron and hole pairs, and facilitating effective interaction between CO$_2$ and reactive centers for redox reactions. A desirable photocatalyst can be a semiconductor[8] or mesoporous materials.[9] A new class of hybrid porous materials with extended two-dimensional (2D) or three-dimensional (3D) crystal structures are metal−organic frameworks (MOFs), which are composed of metal ions or clusters referred to as secondary building units (SBUs) linked with organic ligands (organic linkers). MOFs exhibit large specific surface areas and tunable pore size and structural diversity through functionalization of organic ligands. Therefore, they have attracted great attention for a variety of potential applications in numerous areas such as chemical separation,[10] biomedical sensing,[11] catalysis,[12] drug delivery,[13] gas separation and storage,[14] and other areas.[15] MOFs offer an ideal platform to convert CO$_2$ into chemical feedstock and they can simulate the photosynthetic systems. The CO$_2$ adsorption capacity of MOF materials is due to their good pore size, surface characteristics, and porous functionalities. Furthermore, by introducing catalytic sites, namely, transition metals, into MOF structures, the activation of CO$_2$ is efficiently performed, and the process of CO$_2$ reduction will develop. Also, the photocatalytic properties of MOF materials can be improved by inserting photoactive catalytic sites into MOFs. One of the liable strategies to achieve this goal is to introduce N-rich aromatic ligands such as porphyrins as organic linkers. Facilitating a broad spectrum of light harvesting, long excited state lifetime, and redox activity are some of the most essential characteristics that photocatalysts must have. In addition to these properties, porphyrins possess rich π-electron density; therefore, they exhibit distinct photophysical and electrochemical properties. There have been many attempts to employ porphyrins and metalloporphyrins as organic linkers in

MOF structures, which helps in constructing porous MOFs and boosting the performance of CO_2 photoreduction.

Zr-based MOFs have potent structures and perfect stabilities, which make them a popular class of photocatalytic MOFs. One of the representative examples is MOF-525-Co, which was constructed by integrating Zr_6 clusters with Co-TCPP ligands to prepare MOF-525-Co.[16] The existence of unsaturated Co sites provides adequate active sites, and CO_2 adsorption will increase due to the open sites of Co porphyrins, thereby enhancing the photocatalytic efficiency for CO_2 reduction. Zhang et al. developed a stable mesoporous zirconium−porphyrin MOF, PCN-222, and examined its photocatalytic efficiency for CO_2 conversion under visible-light irradiation.[17] They stated that the porphyrin ligand in PCN-222 serves as a light-harvesting part and it can help enhance CO_2 over catalytic Zr_6 clusters. They also found that improvement of the electron trap state in PCN-222 permits efficient suppression of electron−hole recombination, thereby boosting the photocatalytic activity of the MOF. In addition, a rhodium (III)-porphyrin zirconium metal−organic framework (Rh-PMOF-1(Zr)) photocatalyst has been reported, which can behave as an efficient heterogeneous photocatalyst for CO_2 reduction.[18] Zr^{4+} cations have been used as metal nodes and Rh (TCPP)Cl as organic linkers. Rh-PMOF-1 had the best photocatalytic performance with an $HCOO^-$ yield of 6.1 $\mu mol/ \mu mol_{cat}$ under UV−visible light irradiation for 18 h. In 2019, Qin and co-workers[7] prepared a mixed-ligand MOF (PCN-138) and examined its photocatalytic performance for CO_2 reduction. It benefits from the coexistence of photosensitive porphyrin ligands and Zr-oxo centers in the PCN-138 framework. A mixed-ligand system of symmetric organic ligands, namely, TCPP and BTB (TBTB), was utilized to construct a 3D cage-based MOF. A series of Zr^{IV}-porphyrinic MOFs (ZrPP-n) were synthesized via a top-down fabrication strategy by Bu and co-workers, which exhibited high photocatalytic activity to reduce CO_2 into CO and CH_4 under visible-light irradiation and had both acid and base resistance. ZrPP-n is constructed from porphyrin ligands, including THPP and THBPP linked with Zr oxide rods, and formed a porous network.[19]

The quantitative structure−property relationship (QSPR) method has recently attracted much attention in physical, medicinal, analytical, organic, and inorganic chemistry. The chemical properties or biological activities are related to the molecular structure of a chemical compound. The QSPR modeling applies such a relationship to predict desired activities/properties of new compounds and new products. The QSPR models are constructed by finding the correlation between structure and property and then selecting structures with the desired properties. The QSPR models can use a multilinear regression (MLR) method based on choosing several molecular descriptors. The appropriate descriptors usually are theoretical or extracted from available experimental sources. Validation of the obtained model is performed using a testing set to ensure that the model is fit and effective; then, the best compounds can be synthesized and the desired properties tested in the laboratory.

Herein, we report for the first time the development of a robust QSPR model to estimate the evolution rate of the photocatalytic products of CO_2 conversion of porphyrin-based MOFs conducting CO_2 photoreduction. The proposed model was developed using the MLR method. A data set of some MOFs was used to "train" the QSPR model, and then the

precision of the proposed model was assessed on a "test" set of MOFs. According to the model, it was determined which molecular moieties within MOFs have a significant effect on the photocatalytic activity of CO_2 reduction. Then two MOFs, Cu-PMOF and Co-PMOF, were designed as photocatalysts. Due to the appropriate UV−visible light absorption of the M-TCPP molecule and considering that UV−visible light absorption (Abs.) value is used as one of the main variables in the represented model, Cu-TCPP and Co-TCPP were considered as organic linkers. Moreover, copper and cobalt were selected as the metal node available in MOF structures because they not only show a strong interaction with M-TCPP linkers (one of our most influential variables in the expressed model was the interaction between the metal center and organic ligand) but also possess a high redox potential. As a result, they are proper electron acceptors. Thus, they have good effects on the efficiency of the photocatalytic reaction. After the design, these two MOFs were synthesized and characterized using different techniques. The synthesis of copper (II)- and cobalt (II)-porphyrin metal−organic frameworks (Cu-PMOF, Co-PMOF) from copper and cobalt metalloporphyrins (Cu-TCPP, Co-TCPP) as organic ligands and copper and cobalt SBUs was carried out. These two photocatalysts selectively performed photoreduction of CO_2 to formic acid under UV−visible light irradiation. The characterization of the developed porous MOFs was confirmed using the X-ray diffraction (XRD) technique, diffuse reflectance spectroscopy (DRS), Fourier transform infrared (FTIR), and nitrogen adsorption analysis. The metalloporphyrin units and metal clusters carried out CO_2 photoreduction through two simultaneous catalytic pathways.

2. EXPERIMENTAL SECTION

2.1. Materials. Pyrrole, propionic acid, 4-carboxybenzaldehyde, $Cu(NO_3)_2 \cdot 3H_2O$, and $Co(NO_3)_2 \cdot 66H_2O$ were purchased from Sigma-Aldrich. Solvents were obtained from Sigma-Aldrich and used as received. All reagents except pyrrole were distilled before use. The CO_2 gas of 99% purity was used without further purification.

2.2. Instrumentation. X-ray diffraction (XRD) patterns were collected by a D Jeoljdx-8030 X-ray powder diffractometer using Cu $K\alpha$ (l = 0.154 nm) radiation (40 kV, 30 mA). The Fourier transform infrared (FTIR) spectra were examined in the range of 4500−400 cm^{-1} on a Shimadzu FTIR-8400S spectrophotometer using a KBr pellet. The Brunauer−Emmett−Teller (BET) surface area and pore size distribution were measured with an ASAP 2020 Micromeritics instrument using the multilayer nitrogen adsorption method in a conventional volumetric technique. The samples were degassed under vacuum at 120 °C for 2 h; the N_2 adsorption/desorption isotherms were measured at −196 °C. Diffuse reflectance spectroscopy (DRS) was performed on a Shimadzu (MPC-2200) spectrophotometer from 200 to 1000 nm using barium sulfate ($BaSO_4$) as a standard. The UV−vis absorption spectra were obtained on a Shimadzu UV-1700 spectrophotometer in the wavelength range of 200−800 nm. The products of the reaction were analyzed using high-performance liquid chromatography (HPLC) (LC-2010 PLUS, Shimadzu, Japan) and gas chromatography (GC-7900, CEAULIGHT, China) with a flame ionization detector (FID).

2.3. Computational Methods. An accurate model was developed by selecting four appropriate descriptors, including the dipole moment of solvent (μ), redox potentials (E_{redox}),

Table 1. Experimental and Theoretical Values of Log (Yield) of Porphyrin-Based MOFs for Training (No: 1—16) and Test (No: 17—21) Sets

no.	MOFs entry	μ	E_{redox}	Abs.	Int.$_{M-Por}$	exp. log (yield)[a]	refs	pred. log (yield)[b]	dev.[c]
					Training Set (16 Entries)				
1.	Rh-PMOF-1(Zr)	3.920	0.82	435.738	−0.024	1.646	18	1.642	0.004
2.	PCN-222	3.920	0.82	406.232	−0.132	1.477	17	1.470	0.007
3.	MOF-525-Co	3.920	0.82	406.232	−0.021	0.453	16	0.448	0.005
4.	MOF-525-Zn	3.920	0.82	402.540	−0.006	0.170	16	0.165	0.005
5.	MOF-525	3.920	0.82	405.718	0.034	−0.076	16	−0.082	0.006
6.	MOF-525-Ni	3.051	0.82	406.232	0.009	1.923	5	1.921	0.002
7.	Zn/ PMOF	1.850	0.00	405.718	−0.087	1.018	27	1.011	0.007
8.	ZrPP-1-Co	3.920	0.82	405.672	−0.043	0.632	19	0.627	0.005
9.	ZrPP-1-Fe	3.920	0.82	401.980	−0.004	0.130	19	0.121	0.009
10.	ZrPP-1-Cu	3.920	0.82	405.672	0.027	−0.012	19	−0.019	0.007
11.	ZrPP-1-H2	3.920	0.82	405.158	0.147	−1.143	19	−1.146	0.003
12.	PCN-224(Cu)	1.850	0.00	405.718	0.080	−0.523	28	−0.530	0.007
13.	PCN-223	2.747	0.00	435.770	−0.015	−0.266	29	−0.271	0.005
14.	PCN-224	2.747	0.00	435.770	0.035	−0.725	29	−0.732	0.007
15.	PCN-223(Zn)	2.747	0.00	435.770	−0.021	−0.206	29	−0.215	0.009
16.	PCN-224(Zn)	2.747	0.00	435.770	0.012	−0.518	29	−0.520	0.002
RMSEP:									0.006
					Test Set (5 Entries)				
17.	PCN-138	1.850	0.82	405.718	0.336	1.306	7	1.304	0.002
18.	Zn-MOF[d]	3.387	0.82	406.232	0.161	−0.153	4	−0.159	0.006
19.	ZrPP-1-Zn	3.920	0.82	405.672	0.167	−1.301	19	−1.310	0.009
20.	PMOF	3.051	0.82	436.280	0.3052	0.381	3	0.379	0.002
21.	PCN-222(Zn)	2.747	0.00	435.770	−0.061	0.158	29	0.154	0.004
RMSEP:									0.005

[a]Exp.log (yield): Experimental value of log (yield). [b]Pred.log (yield): Predicted value of log (yield). [c]Dev.: Deviation. [d]Zn-MOF nanosheet.

light absorption values (Abs.) in the UV−visible spectrum, and the interaction between the metal center and porphyrin ligand in the MOF matrix (Int.$_{M-Por}$). These descriptors reflect the molecular properties of MOFs and provide a picture of the chemical nature of photocatalytic characteristics of porphyrin-based MOFs. A data set of porphyrin-based MOF compounds (containing different porphyrin ligands as organic linkers), with experimental information about their photocatalytic activities for CO_2 reduction, was provided and divided into a training and a test set, 80% of data as a training set and 20% as a test set (the 80/20 rule, Pareto's principle) (Table 1).[20] The training set was applied to make an MLR model, and the testing set was used to validate the model. Molecular structures of porphyrin linkers available in MOF structures for training and test sets are listed in Table S1 (Supplementary Information).

Statistical coefficients, R^2 (coefficient of determination) and R_{adj}^2 (the adjusted R-squared) are calculated as the following equations (eqs 1 and 2)

$$R^2 = 1 - \frac{\sum (y_i - \hat{y}_i)^2}{\sum (y_i - \overline{y})^2} \tag{1}$$

$$R_{adj}^2 = 1 - \left[\frac{(1 - R^2)(n - 1)}{n - k - 1} \right] \tag{2}$$

where y_i, $\overline{y}$, and $\hat{y}_i$ are the observed, average, and calculated values of the dependent variable, respectively. The value of n is the number of points in the data sample, and k is the number of independent regressors. If the calculated values y_i and $\hat{y}_i$ have been replaced by the predicted values, the coefficient of

determination for the test set will result, which is expressed by Q^2 (eq 3)

$$Q^2 = 1 - \frac{\sum (y_{itr} - \hat{y}_{itr})^2}{\sum (y_i - \overline{y})^2} \tag{3}$$

where y_{itr} and $\hat{y}_{itr}$ show the observed and the calculated values of the training set, respectively. Other statistical parameters, including three metrics, Q_{F1}^2, Q_{F2}^2, and Q_{F3}^2, are explained by eqs 4−6

$$Q_{F1}^2 = 1 - \frac{\sum (y_i - \hat{y}_i)^2}{\sum (y_i - \overline{y}_{tr})^2} \tag{4}$$

$$Q_{F2}^2 = 1 - \frac{\sum (y_i - \hat{y}_i)^2}{\sum (y_i - \overline{y}_{test})^2} \tag{5}$$

$$Q_{F3}^2 = 1 - \frac{\sum (y_i - \hat{y}_i)^2 / n_{test}}{\sum (y_i - \overline{y}_{tr})^2 / n_{tr}} \tag{6}$$

where the test subscript indicates that the corresponding parameter is related to the test set. The model accuracy is defined by the concordance correlation coefficient (CCC), which is demonstrated by eq 7 as follows

$$Q_{CCC}^2 = \frac{\sum (y_i - \overline{y})(\hat{y}_i - \overline{\hat{y}})}{\sum (y_i - \overline{y})^2 + \sum (\hat{y}_i - \overline{\hat{y}})^2 + \sum (\overline{y} - \overline{\hat{y}})^2} \tag{7}$$

As mentioned earlier, in this work, the product evolution rate of the photocatalytic reduction of CO_2 over porphyrin-based MOFs as photocatalysts was predicted by a BMLR model;

Scheme 1. Schematic Setup for Photocatalytic CO$_2$ Reduction
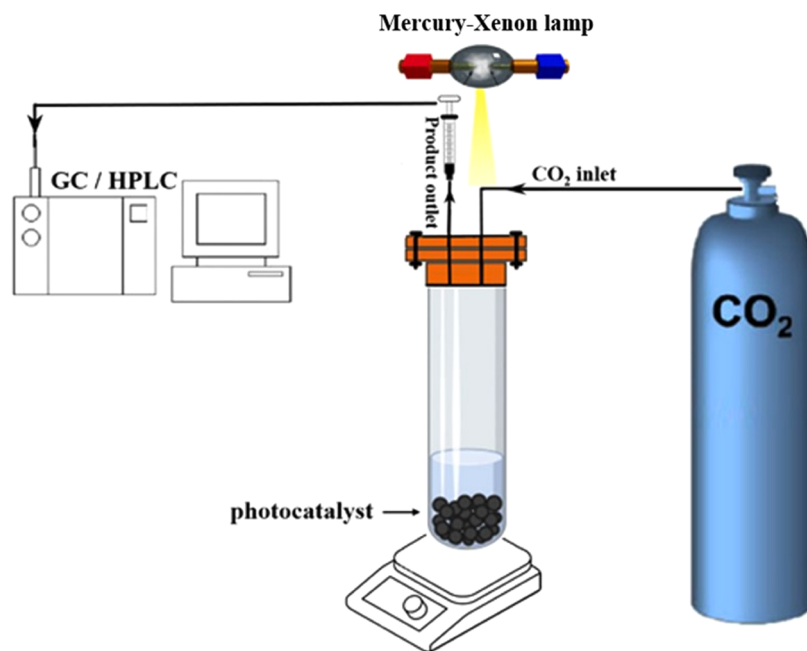
therefore, the yield of products in μmol was considered as the dependent variable (y) in the presented model, and it is expressed in log (yield).

2.4. Preparation of Photocatalysts. Two photocatalysts, Cu-PMOF and Co-PMOF, were synthesized as described below.

2.4.1. Synthesis of TCPP (Tetrakis(4-carboxyphenyl)-porphyrin). The TCPP was synthesized according to the method reported previously.[21] First, 180 mL of propionic acid was heated to refluxing temperature, and 9 mmol of 4-carboxybenzaldehyde was added; then, 8.94 mmol of distilled pyrrole was added dropwise to the solution and refluxed for 1 h. After 72 h of rest, the obtained solid was filtered and washed with ethanol. The resultant purple porphyrin (TCPP) was dried at 60 °C.

2.4.2. Synthesis of Cu-PMOF. Cu-PMOF was prepared via a solvothermal treatment, similar to MMPF-9,[22] except that tdcbpp was replaced by tetrakis(4-carboxyphenyl)porphyrin (TCPP). A blend of TCPP (0.04 mmol) and Cu(NO$_3$)$_2$·3H$_2$O (0.4 mmol) was dissolved in a 20 mL mixed solvent (16 mL of formic acid and 4 mL of N,N-dimethylformamide (DMF)) using ultrasonication at room temperature. The mixture was transferred and sealed in a Teflon-lined stainless-steel autoclave and maintained at 75 °C for 72 h. Dark red crystals were obtained, and then the resultant crystals were washed with DMF and dried at room temperature.

2.4.3. Synthesis of Co-PMOF. Co-PMOF also was prepared similar to MMPF-2[23] by a solvothermal treatment, but H$_{10}$tdcpp was replaced by tetrakis(4-carboxyphenyl)porphyrin (TCPP). A mixture of TCPP (0.02 mmol) and Co(NO$_3$)$_2$·6H$_2$O (0.2 mmol) was dissolved in a 20 mL mixture solvent (13.3 mL of DMA (dimethylacetamide), 3.3 mL of MeOH, 3.3 mL of H$_2$O) using ultrasonication. Then, the solution was placed and sealed in a Teflon-lined stainless-steel autoclave before heating at 115 °C for 24 h. The obtained crystals were collected and washed with DMA and dried at room temperature.

2.5. Photocatalytic Reaction. Twenty milligrams of the photocatalyst was treated under vacuum at 50 °C for 12 h and then placed into a closed vessel. The photocatalyst was dispersed in a 10 mL solution of H$_2$O and triethanolamine (TEOA) (4/1: v/v). The photocatalytic system was purged with pure CO$_2$ for 30 min, and then the photocatalytic reaction was carried out under a CO$_2$ atmosphere. The mixture was irradiated with a 150 W mercury−xenon lamp (UV−visible wavelength range) at room temperature with continuous stirring. After 8 h of irradiation, the amount of HCOOH in the liquid phase was detected using HPLC, and the gaseous phase was analyzed using gas chromatography. No signals for CH$_4$ and CO were observed. The schematic setup of the photocatalytic system is shown in Scheme 1.

3. RESULTS AND DISCUSSION

3.1. QSPR Modeling. A reliable and extensible correlation for predicting the yield of CO$_2$ reduction on MOFs as photocatalysts were performed in this research. To build a BMLR model, four variables, including the dipole moment of solvent (μ), redox potentials of used electron donor (E_{redox}), light absorption values (Abs.) in the UV−visible spectrum for porphyrin molecules available in MOF, and the interaction between the metal center and porphyrin ligand in the MOF matrix (Int.$_{M-Por}$), were applied by the best fit to experimental data (eq 8).

$$\log \text{(yield)} = -10.678 - 1.942\,\mu + 4.887\,E_{redox} + 0.0358$$

$$\text{Abs.} - 9.199\,\text{Int.}_{M-Por} \qquad (8)$$

The product yield of CO$_2$ photoreduction is expressed as log (yield) for ease of computation. The Abs. and Int.$_{M-Por}$ values were used to derive adjustable parameters based on the MLR method. Abs. shows the contribution of absorption of porphyrins in the UV−visible region and Int.$_{M-Por}$ indicates the interaction between the metal node and porphyrinic ligand. According to the proposed model, μ, i.e., the dipole moment of the solvent used in the reaction medium, and E_{redox}, the redox
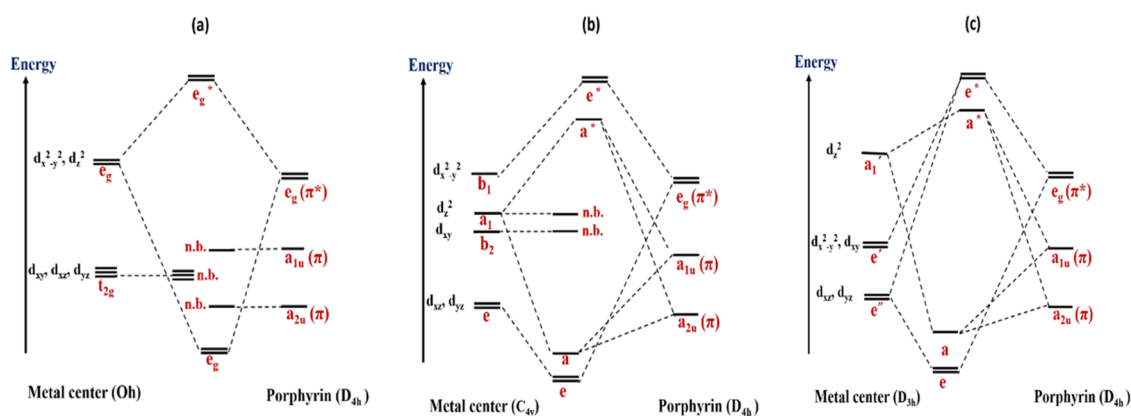
Figure 1. Molecular orbital diagram indicating the interaction between metal d orbitals and porphyrin frontier orbitals for the geometry of the metal center: (a) O_h, (b) C_{4v}, and (c) D_3h.

Table 2. Correlation Parameters for Validation of Equation 8 by the Training and Test Sets

method	sets	R^2	$R^2_{adj.}$	Q^2	Q^2_{F1}	Q^2_{F2}	Q^2_{F3}	Q^2_{CCC}
equation 8	training set	0.999	0.999	0.999949				
	test set	1.000	1.000	1.000	0.99996	0.99996	0.9585	0.99794

potential of the electron donor employed in the photoreduction of CO_2, are suitable descriptors for estimating the product yield of CO_2 reduction. In this study, it was observed that in the collected data set (Table 1), either TEOA was used as an electron donor or no electron donor was used; therefore, the E_{redox} value of 0.82 (the redox potential of TEOA) or zero was considered. Based on the coefficients of Abs. and Int.$_{M-Por}$ specified in eq 8, Abs. and Int.$_{M-Por}$ are called increaser and decreaser parameters, respectively, because these parameters can increase and decrease the log (yield). The exact values of these variables are adjusted based on statistical parameters and obtained by maximizing the value of R^2 and minimizing the value of root-mean-square error (RMSE). Further to present the model, the yields of photoreduction reactions expressed in μmol were considered regardless of what type of products were obtained because it seems that some reaction conditions (such as the phase in which the reaction was conducted) and the product type did not have much effect on the reaction yield prediction equation rather the parameters including μ, E_{redox}, Abs., and Int.$_{M-Por}$ had the greatest effects on the prediction of the yield.

The contribution to UV−visible absorption of porphyrin parts by MOFs is shown by Abs., which was obtained from our previous investigation.[24] The study of absorption of porphyrins and metalloporphyrins confirmed that there is a reliable correlation based on their structural parameters, according to eq 9

$$\text{Abs.} (/nm) = 414.28 + 0.14 n_C + 36.92\, \text{Abs}_{metal} + 33.96$$

$$\text{Abs}_{metal-free} \qquad (9)$$

where n_C is the number of carbon atoms of the desired porphyrin derivatives, Abs_{metal} is the contribution of the interactions between the metal and porphyrins in metalloporphyrins and ligand-coordinated metalloporphyrins, $\text{Abs}_{metal-free}$ is the correction factor for the existence of some specific substituents attached to porphyrin.

The Abs. values of porphyrin moieties within MOFs (Table S1) were acquired from eq 9, and it was found that the Abs.

value has an appreciable effect in predicting log (yield). Table 1 presents the resulting Abs. values.

To specify the Int.$_{M-Por}$ value, the geometry of the metal center and the symmetry of the ligand should be considered; the symmetry of porphyrins or metalloporphyrins is D_{4h}, while the geometric structures surrounding metal nodes in MOF structures are diverse (octahedral, dodecahedral, square pyramidal, trigonal prism, trigonal bipyramidal). Therefore, the splitting of the d orbitals of metals will be varied. The Int.$_{M-Por}$ values for the studied MOFs were determined from the interaction between metal d orbitals and porphyrin ligands, considering our previous inorganic chemistry knowledge.[24−26] In the collected data set, there are three types of point groups for the geometric structures of the metal centers, including O_h, C_{4v}, and D_3h. Considering the symmetry of metal centers, the interaction between the metal frontier orbitals and ligand group orbitals (porphyrin) builds three molecular orbital diagrams (Figure 1).

Depending on the metal type available in a metal node and the geometry of the metal center, different Int.$_{M-Por}$ values will be obtained through tedious work. In addition, the Int.$_{M-Por}$ value depends on whether the metal node interacts with a porphyrin or a metalloporphyrin linker. Moreover, for metalloporphyrin linkers, the different metals available in metalloporphyrin lead to various amounts of Int.$_{M-Por}$ value. Besides, metal cluster units may be connected by different numbers of porphyrin linkers. The number of porphyrin linkers bridging the metal clusters (different framework topology) will affect Int.$_{M-Por}$. The calculated values of Int.$_{M-Por}$ for training and test sets are listed in Table 1.

The Int.$_{M-Por}$ value as an adjusted parameter can be determined using crystal field and molecular orbital theory. The interaction values of some interacting moieties have previously been calculated for different metals and ligands.[24,26,30] By considering these basic numerical values and placing these basic values in the proposed model, the exact value of Int.$_{M-Por}$ will be obtained. The basic numerical values are adjusted and then cross-values are evaluated in the model, thus maximizing the value of R^2 and minimizing the value of root-mean-square error (RMSE).

From the resulting BMLR model (eq 8), both R^2 and adjusted R^2 values were 0.999 for training sets. Table 2 indicates that the predictive squared correlation coefficients (Q^2), including Q_{F1}^2, Q_{F2}^2, Q_{F3}^2, and Q_{CCC}^2, of the model obtained were 0.99996, 0.99996, 0.9585, and 0.99794, respectively; these statistical parameters deal with the validity of the model.

Another statistical parameter, RMSEP, obtained were 0.0063 and 0.0055 for training and test sets, respectively (Table 3). The low values of RMSEP ascertain that a suitable model was achieved for estimating the yield of CO_2 reduction reaction on MOF photocatalysts.

Table 3. Statistical Parameters for the Training and Test Sets

equation 8	no. of data	RMSEP	R^2
training set	16	0.0063	0.999
test set	5	0.0055	1.000

Figure 2 displays the prediction and the experimental values of the evolution rate of CO_2 reduction. From the plot, it is
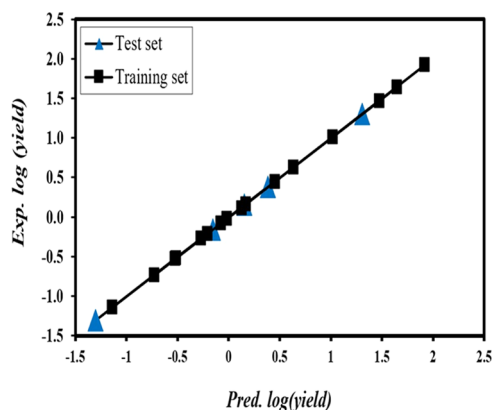

Figure 2. Experimental values of the evolution rate of CO_2 reduction for training and test sets versus the predicted values.

apparent that the predicted values of the product evolution rate are fitted on experimental values.

To validate a QSPR model, the cross-validation method is used as a popular validation technique. In this study, leave-one-out, leave-many-out, and y-randomization procedures were employed for this purpose. Leave-one-out cross-validation (LOOCV) is a type of cross-validation similar to k-fold cross-validation, but the number of folds equals the number of instances in the data set ($k = n$), and its purpose is to predict that one held-out data. LOOCV is often used when the size of the data set is small and consecutively presents models with training sets leaving out one data point, thereupon averaging the prediction errors. Leave-many-out (LMO) cross-validation is performed by removing numbers of data in each step, and the MLR models are developed based on the remaining data. The y-randomization test is known as a validation method that compares the proposed model's R^2 with the models' R^2 built for randomly shuffled responses. For the y-randomization test, several runs are performed in which the original descriptor matrix X is considered constant, and the vector y is randomized. Then, it can be determined whether the model is characterized by chance correlation or not. If $R_{yrand}^2 > 0.5$, it

is known as chance correlation.[31] In this work, to confirm the model's effectiveness in predicting the yield of CO_2 photoreduction reactions, R_{LOO}^2, R_{LMO}^2, and R_{yrand}^2 were calculated, and the values of 0.9204, 0.9992, and 0.49 were obtained, respectively, for these statistical parameters.

Based on the collected data, it was found that the interaction between the metal node and porphyrin ligand ($Int._{M-Por}$) is a significant parameter for developing a model to predict the yield of CO_2 reduction on MOF photocatalysts. When copper and cobalt are selected as metal nodes, the yield of the reaction will be optimum. On the other hand, copper and cobalt provide very strong and specific interactions with Cu-TCPP and Co-TCPP as porphyrin linkers. Moreover, these two linkers have appropriate absorptions in the UV−visible region (Abs. value), thereby designing two porphyrin-based MOFs: (a) using a copper node and Cu-TCPP linker (Cu-PMOF) and (b) using a cobalt node and Co-TCPP linker (Co-PMOF). After designing, based on the obtained equation (eq 8), the yields of photoreduction of CO_2 over these two MOFs as photocatalysts were evaluated, and it was concluded that they could produce a higher yield than other MOFs in the data set. As a result, these two MOFs were experimentally synthesized and then applied for the photoreduction of CO_2. It was observed that there is a small difference between the experimental yields of CO_2 reduction and theoretical (predicted) values.

3.2. Synthesis and Structure. Tetrakis(4-carboxyphenyl) porphyrin (TCPP) was prepared according to the reported procedure;[21] the UV−visible spectra of TCPP showed a λmax at 418 nm (Soret band) and four Q bands at 514, 549, 591, and 646 nm (Figure 3). The FTIR spectrum of TCPP is
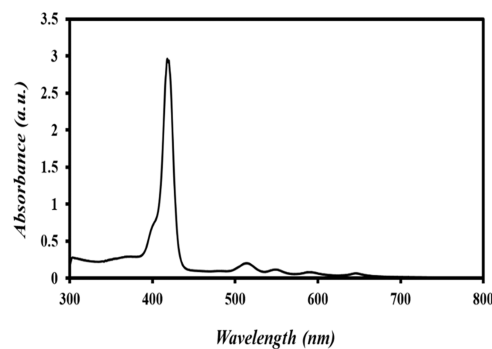

Figure 3. UV−visible absorption spectrum of TCPP porphyrin.

illustrated in Figure 4c. The peak around 1000−1300 cm^{-1} indicates the presence of $=C-N$ in the porphyrin structure, the peak at 1595 cm^{-1} is due to the presence of stretching vibration of the aromatic $C=C$ bond, the peaks that fall around 1629 and 1675 cm^{-1} are related to $-C=N$ of pyrrole, and the appearance of a peak at 3400 cm^{-1} could be attributed to NH groups in the porphyrin structure.

Similar to the method reported by Ma et al.,[22,23] a solvothermal method was used to prepare the Cu-PMOF and Co-PMOF crystals. The Cu-PMOF was synthesized via assembly of $Cu(NO_3)_2 \cdot 3H_2O$ and TCPP in formic acid and DMF, while the Co-PMOF was prepared by adding $Co(NO_3)_2 \cdot 6H_2O$ to the TCPP, DMA, methanol, and H_2O solution. Thus, the resultant MOFs are expected to show similar properties to their parent MOFs. Under the reaction conditions, the TCPP could be metalized by Cu^{2+} and Co^{2+}
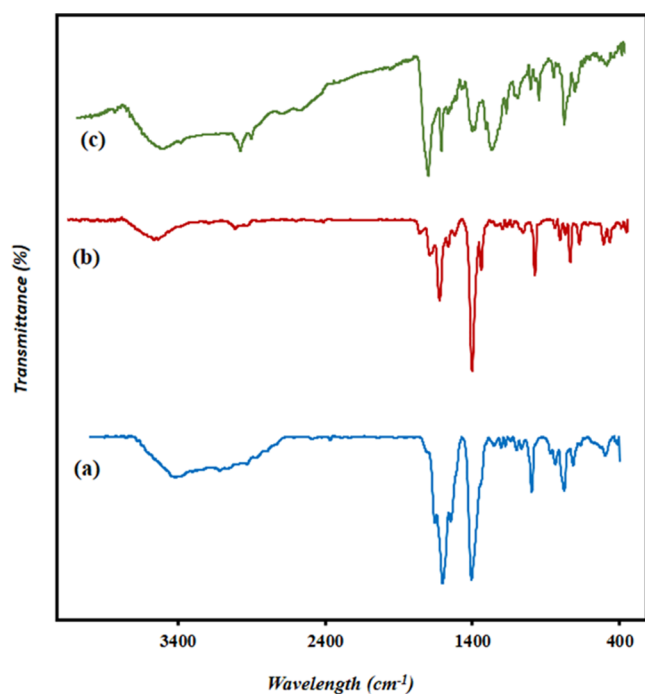
Figure 4. FTIR spectra of (a) Cu-PMOF, (b) Co-PMOF, and (c) TCPP.

ions, respectively (Figure 5). The TCPP ligand was used as a linker in the porphyrin-based MOFs because it has four accessible carboxylate groups. Thereby, the linkage between the linker and metal SBUs is easily achieved. The FTIR spectra of Cu-PMOF and Co-PMOF are displayed in Figure 4, which exhibits the typical and characteristic peaks of these compounds and indicates the peaks' assignment in the graph. The peak at 720 cm^{-1} is due to the CH group of meso phenyl in Cu-PMOF and Co-PMOF; the peaks around 1370 and 1630 cm^{-1} indicate the presence of $=$C$-$N and C$=$N in Co-PMOF, respectively. The appearance of the peak at 2869 cm^{-1} is attributed to the stretching vibration of the C$-$H bond. As

can be seen in Figure 4a,b, the presence of the bands at about 3429 cm^{-1} could be attributed to the O$-$H and N$-$H stretching vibrations for Cu-PMOF and Co-PMOF. Furthermore, the peak at 964 cm^{-1} attributed to the N$-$H in the pyrrole ring, which then shifted to around 1000 cm^{-1}. This confirms the successful metalation of porphyrin TCPP.[32] Moreover, compared to the FTIR spectrum of TCPP, the intensity of the peak at 3400 cm^{-1} for Cu-PMOF and Co-PMOF has greatly decreased, confirming the formation of Cu$-$N and Co$-$N in Cu-PMOF and Co-PMOF, respectively.

The successful synthesis of Cu-PMOF and Co-PMOF in porous crystalline frameworks was proved by their XRD patterns (Figure 6). The phase purity of the bulk MOFs verified by these studies shows little contamination. Moreover, these XRD patterns are in good agreement with the reference sample patterns. Indeed, the synthesis method of Cu-PMOF was similar to MMPF-9,[22] except that the organic linker was changed, and instead of tdcbpp, TCPP was used; therefore, it was expected that the structure of Cu-PMOF was similar to that of MMPF-9. The XRD patterns prove this fact, and all of the essential peaks in the MMPF-9 pattern can also be observed in the Cu-PMOF pattern. Co-PMOF also was synthesized by a solvothermal method similar to that of MMPF-2,[23] but H$_{10}$tdcpp was replaced by TCPP as the organic linker. The XRD pattern of Co-PMOF was the same as the MMPF-2 pattern as the reference material; all of the major peaks in the MMPF-2 pattern can also be seen in the Co-PMOF pattern, indicating that Co-PMOF was successfully synthesized.

The permanent porosity of Cu-PMOF and Co-PMOF was investigated by N$_2$ adsorption isotherms displayed in Figure 7. For Cu-PMOF, with a nitrogen gas uptake of 214.28 cm^3·g^{-1} (STP), BET surface area was 932.64 m^2·g^{-1}, while Co-PMOF showed a high BET surface area of 974.06 m^2·g^{-1}, and its N$_2$ uptake was ~223.79 cm^3·g^{-1} at STP. Besides, the calculated total pore volume of Cu-PMOF and Co-PMOF was as large as 0.6173 and 0.7853 cm^3·g^{-1}, respectively. The high specific surface area of Cu-PMOF and Co-PMOF will increase the surface-active sites on photocatalysts, leading to effective
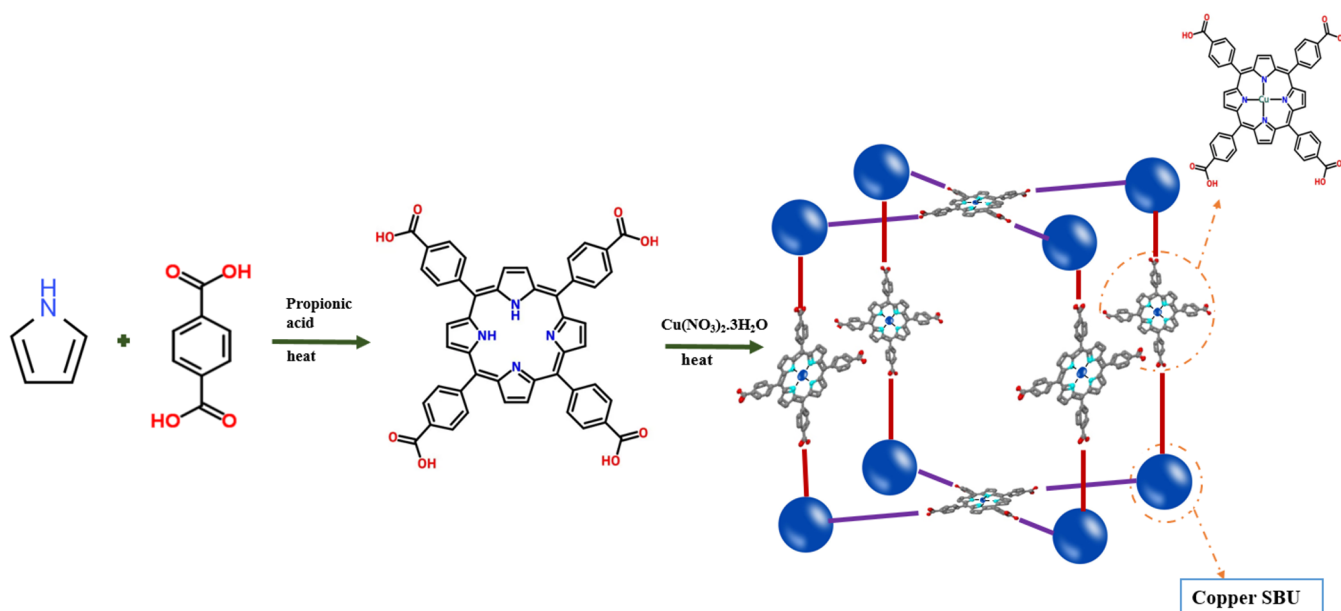

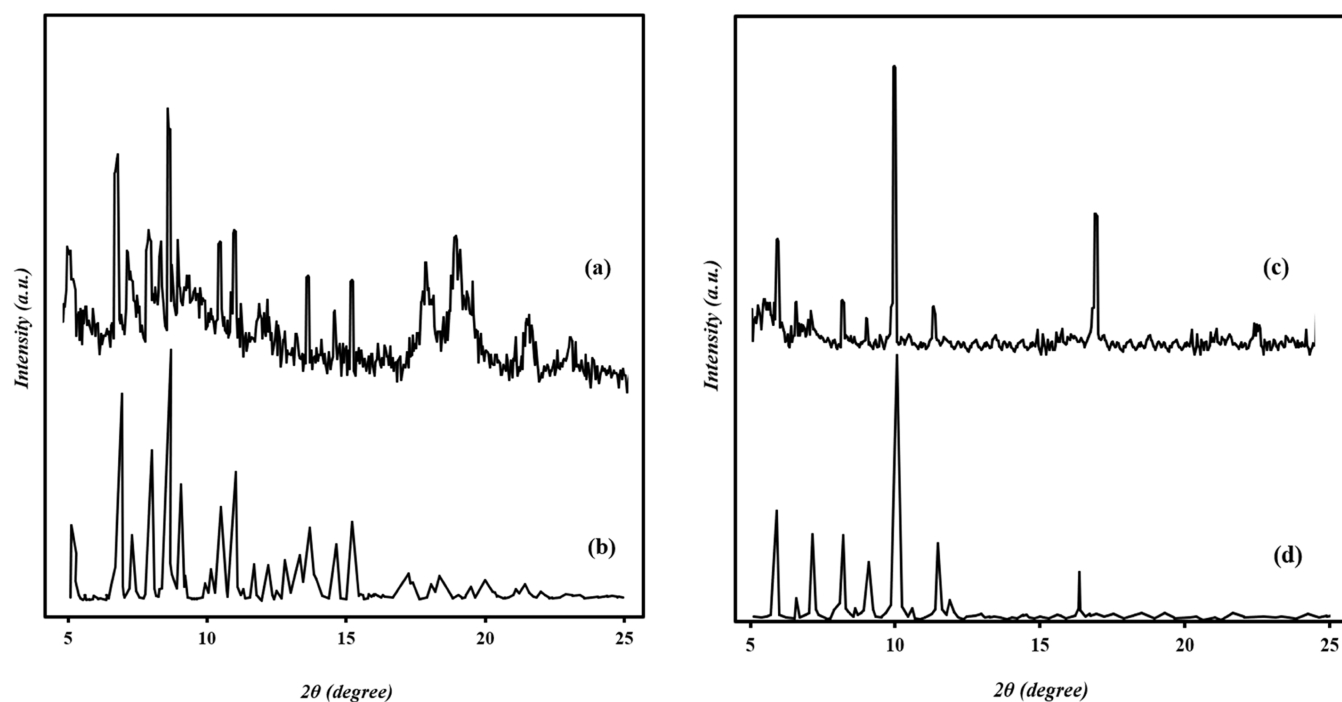**Figure 5.** Schematic synthesis of TCPP and Cu-PMOF.

Figure 6. Powder X-ray diffraction patterns of (a) as-synthesized Cu-PMOF, (b) the reference sample for Cu-PMOF (MMPF-9), (c) as-synthesized Co-PMOF, and (d) the reference sample for Co-PMOF (MMPF-2).
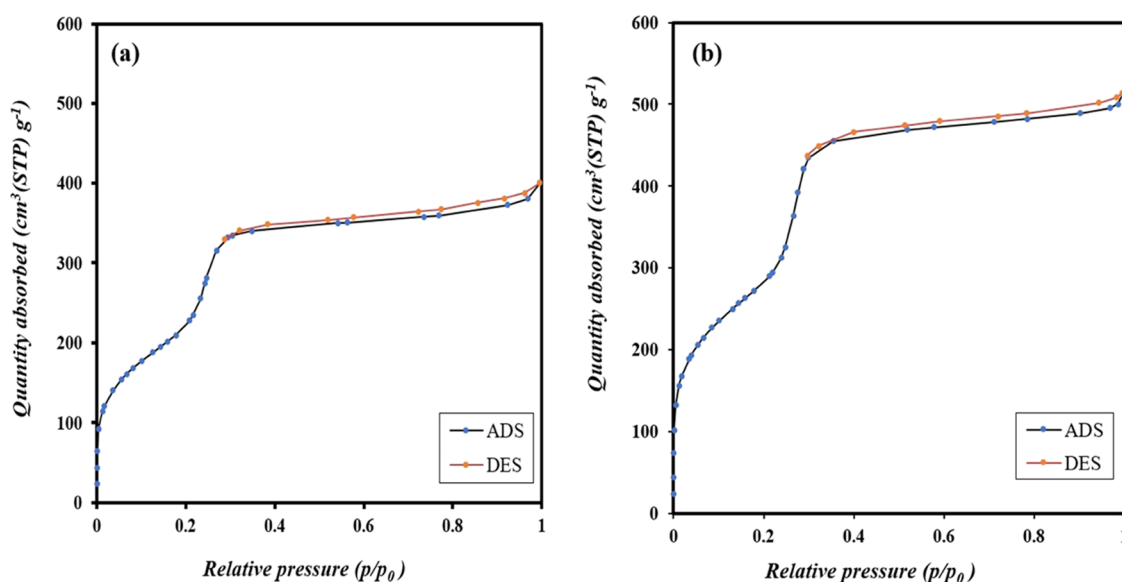

Figure 7. N_2 adsorption−desorption isotherm of (a) Cu-PMOF and (b) Co-PMOF.

adsorption and activation of CO_2 and consequently more efficiency for CO_2 reduction.

UV−visible diffuse reflectance spectroscopy (DRS) studies were conducted, as shown in Figure 8a,b. The UV−visible spectra of Cu-PMOF and Co-PMOF demonstrated a broad absorption band covering the UV−visible region; the absorptions at these wavelengths are effective for harvesting UV−visible light and using these MOFs as photocatalytic systems. Compared to the UV−visible spectrum of TCPP, Co-PMOF displayed a red shift of the Soret band (a common case for metallated porphyrin) and four strong Q bands at 500 to 700 nm, but for Cu-PMOF, only two Q bands were observed. The Tauc plots of MOFs, obtained from drawing $(\alpha h\nu)^{1/2}$

versus the energy $(h\nu)$, are demonstrated in Figure 8c,d. The band gap (E_g) values were obtained from the plot by extrapolating the linear parts using the Kubelka−Munk function. The band gaps of the samples were 2.4 and 5.6 eV for Cu-PMOF and Co-PMOF, respectively.

3.3. Photocatalytic Activity. To study the photocatalytic activity of Cu-PMOF and Co-PMOF, CO_2 photoreduction was conducted in the presence of water and triethanolamine (TEOA) as the reaction solvent and the electron donor, respectively. Moreover, it was performed under UV−visible light irradiation, in the absence of any additional photosensitizer. The reaction setup was purged by pure CO_2 several times to remove any trapped air and oxygen gas. Cu-PMOF
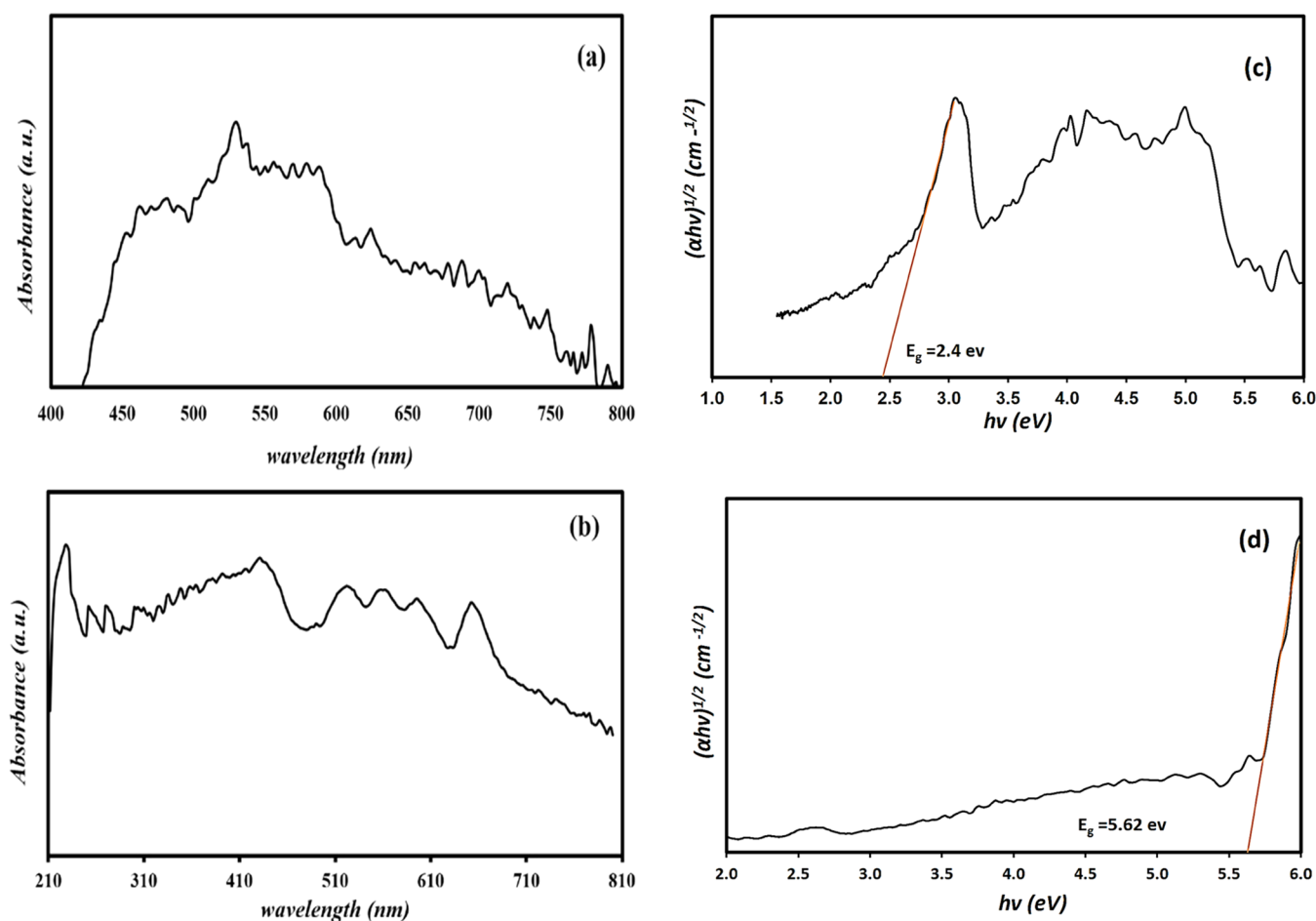
Figure 8. UV−visible diffuse reflectance spectroscopy (DRS) of (a) Cu-PMOF, (b) Co-PMOF, and the Tauc plots of (c) Cu-PMOF and (d) Co-PMOF.

and Co-PMOF showed excellent catalytic activity for CO_2 reduction to formic acid. The concentration of HCOOH was detected and quantitatively analyzed by HPLC. As shown in Figure 9, the amount of produced HCOOH increased with the irradiation time and reached 816.275 μmol·g^{-1}·h^{-1} in 8 h (yield: 130.6 μmol) for Cu-PMOF, while Co-PMOF showed an HCOOH evolution rate of 646.728 μmol·g^{-1}·h^{-1} (yield: 103.476 μmol) under light illumination for 8 h.
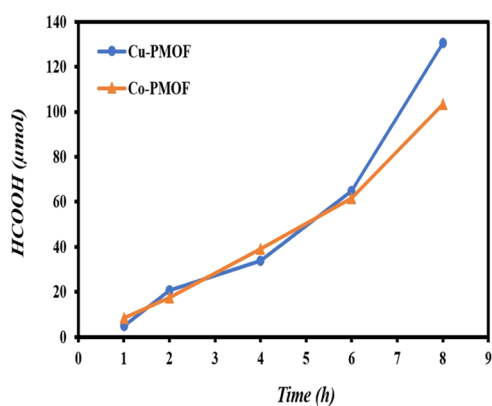

Figure 9. Amount of HCOOH (μmol) produced as a function of time, over Cu-PMOF and Co-PMOF as photocatalysts (20 mg); 10 mL of solvent and TEOA (4/1: v/v); mercury−xenon light (150 W).

According to the model (eq 8), the predicted values of log (yield) for Cu-PMOF and Co-PMOF were calculated to be 2.107 and 2.007, respectively, and the experimental values of log (yield) were obtained to be 2.116 and 2.015, respectively. For Cu-PMOF: log (yield) = −10.678 − 1.942 × 1.85 + 4.887 × 0.82 + 0.0358 × 405.718 − 9.199 × 0.2501 = 2.107

For Co-PMOF: log (yield) = −10.678 − 1.942 × 1.85 + 4.887 × 0.82 + 0.0358 × 406.232 − 9.199 × 0.262 = 2.007

A series of controlled experiments (Table 4) were conducted to study the influences of other factors during photocatalytic CO_2 reduction reactions: (1) applying N_2 instead of CO_2 as a

Table 4. Amount of the Produced Formic Acid for Photocatalytic CO_2 Reduction over Different Controlled Experiments after 8 h Light Irradiation

entry	photocatalyst	time (h)	HCOOH (μmol)	selectivity (%)
1	Cu-PMOF	8	130.6	100
2	Co-PMOF	8	103.47	100
3	free TCPP ligand	8	17.06	100
4[a]	dark	8	n.d.	
5[b]	no photocatalyst	8	n.d.	
6[c]	no TEOA	8	n.d.	
7[d]	no CO_2	8	n.d.	

[a]performing CO_2 reduction in the dark;. [b]without photocatalysts;. [c]in the absence of TEOA;. [d]using N_2 instead of CO_2 as a reactant.

reactant under similar conditions, the results showed that no HCOOH can be detected, verifying that the origin of HCOOH is CO_2; (2) performing CO_2 reduction in the dark indicated that no HCOOH can be generated; (3) performing CO_2 reduction under UV–visible light irradiation, but without photocatalysts, also indicated that no detectable products were formed, demonstrating the photocatalytic roles of Cu-PMOF and Co-PMOF in the reduction of CO_2; (4) employing a free TCPP ligand as a photocatalyst to reduce CO_2 under similar conditions, a trace amount (17.06 μmol) of HCOOH was obtained after 8 h, suggesting that photocatalytic activity of TCPP could be significantly improved when porphyrin is introduced within the MOF skeleton to form a porphyrin-based MOF; and (5) conducting the photoreduction of CO_2 in the absence of TEOA showed that no HCOOH can be observed, demonstrating its critical role in the reaction as an electron donor. The selectivity of HCOOH evolution, with Cu-PMOF and Co-PMOF, was also another important feature of these photocatalysts during CO_2 conversion, as no other products were detected in the gas or liquid phases.

To investigate the stability of Cu-PMOF and Co-PMOF, these heterogeneous catalysts can be easily isolated from the reaction media by centrifugation. Next, they can be reused for three cycles (Figure 10). The results showed that these MOFs are not proper recyclable photocatalysts since the rate of produced HCOOH declined during the second and third runs of reaction.
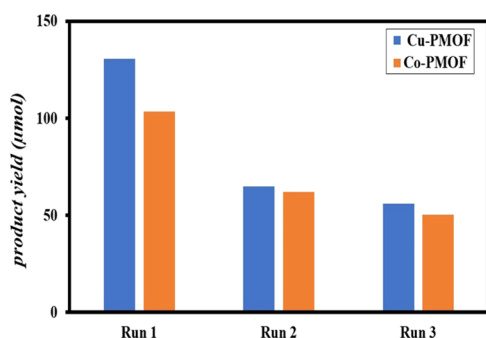

Figure 10. Amount of HCOOH (μmol) produced in three cycles (8 hours for each cycle) over Cu-PMOF and Co-PMOF as photocatalysts.

To determine the stability of Cu-PMOF and Co-PMOF during photocatalysis reactions, the XRD patterns of photocatalysts were acquired after 8 hours of reaction (Figure 11). The XRD patterns of the recovered MOFs exhibited similarities compared with the XRD patterns of the original structures, and only slight changes in the diffraction patterns were observed, suggesting their structural stability.

3.4. Reaction Mechanism. A molecular catalyst can be employed to overcome the thermodynamic barriers of CO_2 reduction associated with fast kinetics and producing stable products. In other words, the reduction of CO_2 by one electron to form $CO_2^{\bullet-}$ is difficult because of the kinetic barriers due to the structural difference between the linear CO_2 molecules and the intended $CO_2^{\bullet-}$ species. However, there are many achievements in the photocatalytic reduction of CO_2 into HCOOH and CO (the two-electron reduction products of CO_2). The MOF photocatalysts stand as a primary area of research because they may act as both the light-harvesting and the catalyst platform. Moreover, by ligand modification, the

potential required for CO_2 reduction can be easily achieved. As mentioned above, one promising strategy for enhancing the CO_2 reduction activity of MOFs is to introduce N-rich aromatic ligands such as porphyrins as linkers in the MOF structures owing to their proper integration of photosensitizer, catalytic activity, and stability, thus avoiding the need for using any additional photosensitizer.

Based on the results of BET studies, which confirm the presence of large pores within the Cu-PMOF and Co-PMOF frameworks, it seems that CO_2 molecules can easily enter the pores; moreover, based on the UV–vis analysis, we found that metalloporphyrin can absorb UV–vis light, give rise to the excited state, and transfer electrons to the metal clusters. In addition, the band gap (E_g) values were obtained from DRS studies, confirming the semiconductor feature of these porphyrin-based MOFs, in which electron–hole separation and redox reaction can be performed. Many studies have both theoretically and experimentally investigated the photocatalytic activity, which were used to understand the photocatalytic reaction mechanism of CO_2 reduction by Cu-PMOF and Co-PMOF. According to the literature,[33] a reasonable reaction mechanism for photocatalytic CO_2 reduction over Cu-PMOF and Co-PMOF was proposed (Scheme 2). First, the MOFs readily capture carbon dioxide due to their porous structures. The metalloporphyrins available in porphyrin-based MOFs offer units to absorb photons, rise to the excited states, and transfer the generated electrons to metal clusters (Cu^{2+}, Co^{2+}). However, triethanolamine (TEOA) as an electron donor provides electrons to metal cations (Cu^{2+}, Co^{2+}) to produce Cu^+ and Co^+, which then reduce CO_2 to $CO_2^{\bullet-}$ and simultaneously oxidize the metal centers to convert back into original states, Cu^{2+} and Co^{2+}. $CO_2^{\bullet-}$ will combine with a hydrogen atom to produce $HCOO^-$, and then the formate ion will combine with a proton to form formic acid as the final product in such a manner that there is no need to break the C–O bond. In other words, quenching of the excited state of Cu-PMOF or Co-PMOF by TEOA will occur, and then the metal centers reduce CO_2 to $CO_2^{\bullet-}$ and eventually liberate HCOOH. TEOA, as a sacrificial agent, consumes the photoinduced holes available in the valence band of the photocatalyst. In addition, the metalloporphyrin individually can perform the photocatalytic activity and reduce CO_2 to a formate anion. The high yield of formate anions is due to the two simultaneous catalytic pathways of CO_2 photoreduction.

4. CONCLUSIONS

In conclusion, a simple BMLR model has been established to estimate the product evolution rate of CO_2 reduction on porphyrin-based MOF photocatalysts. The QSPR model resulted based on four variables, μ (dipole moment of solvent), E_{redox} (redox potentials), Abs. (UV–visible absorption values), and Int.$_{M-Por}$ (the interaction between the metal center and porphyrin ligand). The Abs. and Int.$_{M-Por}$ descriptors play increaser and decreaser roles and they are adjusted parameters. The model validation is performed by comparing the statistical parameters attained by the training and test sets. The values of R^2 were 0.999 and 1.000 for the training and test sets, respectively. Also, other statistical parameters, including RMSEP, MSE, and MAPE, were satisfactory and confirmed the suitable reliability of the equation of the model. Based on the obtained model, two MOFs, Cu-PMOF and Co-PMOF, were designed. In the next step, these two novel porphyrin-based metal–organic frameworks containing Cu-TCPP and
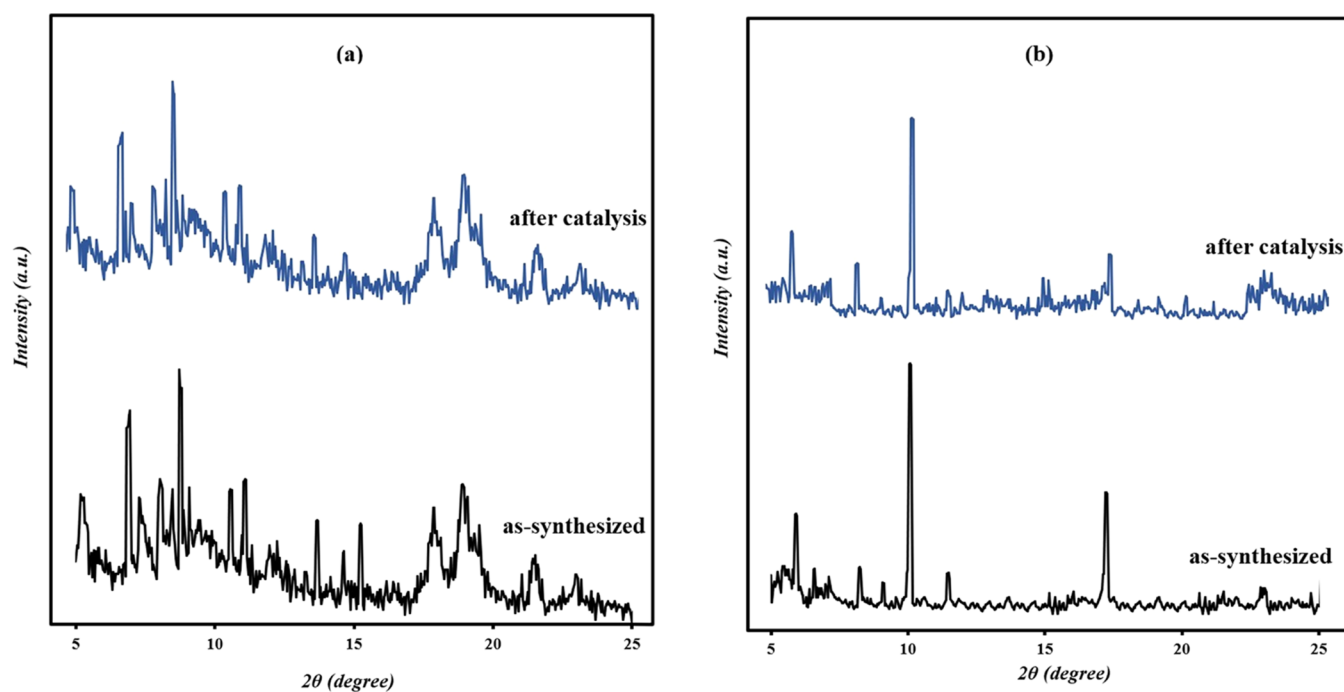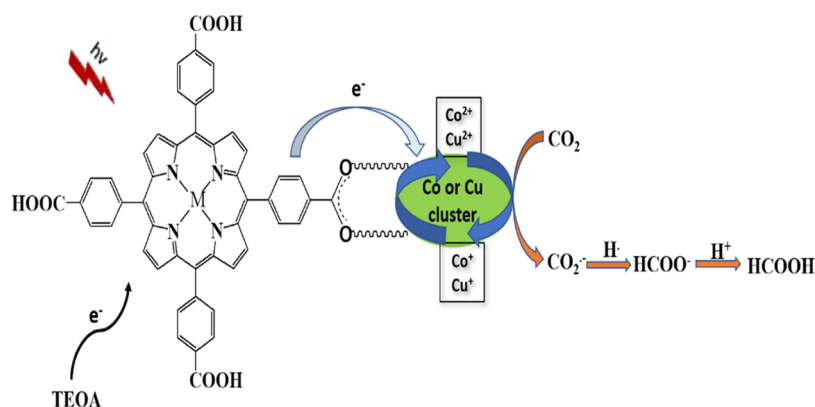
Figure 11. Powder X-ray diffraction patterns of both as-synthesized and after catalysis (a) Cu-PMOF and (b) Co-PMOF.

Scheme 2. Proposed Mechanism of Photocatalytic Reduction of CO_2 to HCOOH over Cu-PMOF and Co-PMOF

Co-TCPP were synthesized as photocatalysts with the highest yield and developed for the photoreduction of CO_2 under UV−visible irradiation. These heterogeneous photocatalysts, which were highly porous and stable, exhibited high photocatalytic efficiency and selectivity for HCOOH evolution. The MOFs mentioned above possess good crystallinity and porosity, as evidenced by the XRD and N_2 adsorption−desorption studies. The obtained results from photoreduction experiments indicated that the amounts of produced HCOOH over Cu-PMOF and Co-PMOF were 130.6 and 103.47 μmol after 8 h, respectively. Incorporating porphyrin moieties within the MOF matrix can improve photocatalytic reduction of CO_2 into formic acid since the porphyrins and metalloporphyrins have excellent light-harvesting ability and electron transfer potency, thereupon enhancing their photocatalytic performances.

■ ASSOCIATED CONTENT

ⓢ Supporting Information

The Supporting Information is available free of charge at https://pubs.acs.org/doi/10.1021/acsomega.2c03724.

Molecular structures of porphyrin linkers available in MOF structures for training and test sets (PDF)

■ AUTHOR INFORMATION

Corresponding Authors

Rahmatollah Rahimi − *Department of Chemistry, Iran University of Science and Technology, 16846-13114 Tehran, Islamic Republic of Iran;* ⦿ orcid.org/0000-0003-4459-0578; Phone: +98-21-73228322; Email: Rahimi_Rah@iust.ac.ir; Fax: +98-021-77491204

Ali Reza Akbarzadeh − *Department of Chemistry, Iran University of Science and Technology, 16846-13114 Tehran, Islamic Republic of Iran;* ⦿ orcid.org/0000-0003-4641-9352; Phone: +98-21-73228318; Email: a_akbarzaeh@iust.ac.ir; Fax: +98-021-77491204

Author

   Leila Tayebi — *Department of Chemistry, Iran University of Science and Technology, 16846-13114 Tehran, Islamic Republic of Iran*

Complete contact information is available at:
https://pubs.acs.org/10.1021/acsomega.2c03724

Notes

The authors declare no competing financial interest.
Figures were inserted in this article after they mentioned related equipment and software.

■ REFERENCES

(1) (a) Peters, G. P.; Andrew, R. M.; Canadell, J. G.; Friedlingstein, P.; Jackson, R. B.; Korsbakken, J. I.; Le Quéré, C.; Peregon, A. Carbon dioxide emissions continue to grow amidst slowly emerging climate policies. *Nat. Clim. Change* **2020**, *10*, 3−6. (b) Morris, A. J.; Meyer, G. J.; Fujita, E. Molecular approaches to the photocatalytic reduction of carbon dioxide for solar fuels. *Acc. Chem. Res.* **2009**, *42*, 1983−1994.

(2) Liu, Y.; Yang, Y.; Sun, Q.; Wang, Z.; Huang, B.; Dai, Y.; Qin, X.; Zhang, X. Chemical adsorption enhanced CO_2 capture and photoreduction over a copper porphyrin based metal organic framework. *ACS Appl. Mater. Interfaces* **2013**, *5*, 7654−7658.

(3) Zheng, C.; Qiu, X.; Han, J.; Wu, Y.; Liu, S. Zero-dimensional-g-CNQD-coordinated two-dimensional porphyrin MOF hybrids for boosting photocatalytic CO_2 reduction. *ACS Appl. Mater. Interfaces* **2019**, *11*, 42243−42249.

(4) Ye, L.; Gao, Y.; Cao, S.; Chen, H.; Yao, Y.; Hou, J.; Sun, L. Assembly of highly efficient photocatalytic CO2 conversion systems with ultrathin two-dimensional metal−organic framework nanosheets. *Appl. Catal., B* **2018**, *227*, 54−60.

(5) Huang, N.-Y.; Zhang, X.-W.; Xu, Y.-Z.; Liao, P.-Q.; Chen, X.-M. A local hydrophobic environment in a metal−organic framework for boosting photocatalytic CO_2 reduction in the presence of water. *Chem. Commun.* **2019**, *55*, 14781−14784.

(6) Fu, Y.; Sun, D.; Chen, Y.; Huang, R.; Ding, Z.; Fu, X.; Li, Z. An amine-functionalized titanium metal−organic framework photocatalyst with visible-light-induced activity for CO_2 reduction. *Angew. Chem., Int. Ed.* **2012**, *51*, 3364−3367.

(7) Qiu, Y.-C.; Yuan, S.; Li, X.-X.; Du, D.-Y.; Wang, C.; Qin, J.-S.; Drake, H. F.; Lan, Y.-Q.; Jiang, L.; Zhou, H.-C. Face-sharing archimedean solids stacking for the construction of mixed-ligand metal−organic frameworks. *J. Am. Chem. Soc.* **2019**, *141*, 13841−13848.

(8) Fujiwara, H.; Hosokawa, H.; Murakoshi, K.; Wada, Y.; Yanagida, S.; Okada, T.; Kobayashi, H. Effect of surface structures on photocatalytic CO_2 reduction using quantized CdS nanocrystallites. *J. Phys. Chem. B* **1997**, *101*, 8270−8278.

(9) (a) Jia, W.; Liu, T.; Li, Q.; Yang, J. Highly efficient photocatalytic reduction of CO_2 on surface-modified Ti-MCM-41 zeolite. *Catal. Today* **2019**, *335*, 221−227. (b) Wu, H.-Y.; Bai, H.; Wu, J. C. Photocatalytic reduction of CO_2 using Ti−MCM-41 photocatalysts in monoethanolamine solution for methane production. *Ind. Eng. Chem. Res.* **2014**, *53*, 11221−11227.

(10) (a) Li, J.-R.; Kuppler, R. J.; Zhou, H.-C. Selective gas adsorption and separation in metal−organic frameworks. *Chem. Soc. Rev.* **2009**, *38*, 1477−1504. (b) Bloch, E. D.; Queen, W. L.; Krishna, R.; Zadrozny, J. M.; Brown, C. M.; Long, J. R. Hydrocarbon separations in a metal-organic framework with open iron (II) coordination sites. *Science* **2012**, *335*, 1606−1610.

(11) He, C.; Lu, K.; Lin, W. Nanoscale metal−organic frameworks for real-time intracellular pH sensing in live cells. *J. Am. Chem. Soc.* **2014**, *136*, 12253−12256.

(12) Lee, J.; Farha, O. K.; Roberts, J.; Scheidt, K. A.; Nguyen, S. T.; Hupp, J. T. Metal−organic framework materials as catalysts. *Chem. Soc. Rev.* **2009**, *38*, 1450−1459.

(13) (a) Horcajada, P.; Chalati, T.; Serre, C.; Gillet, B.; Sebrie, C.; Baati, T.; Eubank, J. F.; Heurtaux, D.; Clayette, P.; Kreuz, C.; et al. Porous metal−organic-framework nanoscale carriers as a potential platform for drug delivery and imaging. *Nat. Mater.* **2010**, *9*, 172−178. (b) Sun, C. Y.; Qin, C.; Wang, C. G.; Su, Z. M.; Wang, S.; Wang, X. L.; Yang, G. S.; Shao, K. Z.; Lan, Y. Q.; Wang, E. B. Chiral nanoporous metal-organic frameworks with high porosity as materials for drug delivery. *Adv. Mater.* **2011**, *23*, 5629−5632.

(14) Sculley, J.; Yuan, D.; Zhou, H.-C. The current status of hydrogen storage in metal−organic frameworks—updated. *Energy Environ. Sci.* **2011**, *4*, 2721−2735.

(15) Wang, M.-S.; Guo, S.-P.; Li, Y.; Cai, L.-Z.; Zou, J.-P.; Xu, G.; Zhou, W.-W.; Zheng, F.-K.; Guo, G.-C. A direct white-light-emitting metal-organic framework with tunable yellow-to-white photoluminescence by variation of excitation light. *J. Am. Chem. Soc.* **2009**, *131*, 13572−13573.

(16) Zhang, H.; Wei, J.; Dong, J.; Liu, G.; Shi, L.; An, P.; Zhao, G.; Kong, J.; Wang, X.; Meng, X.; et al. Efficient visible-light-driven carbon dioxide reduction by a single-atom implanted metal−organic framework. *Angew. Chem.* **2016**, *128*, 14522−14526.

(17) Xu, H.-Q.; Hu, J.; Wang, D.; Li, Z.; Zhang, Q.; Luo, Y.; Yu, S.-H.; Jiang, H.-L. Visible-light photoreduction of CO_2 in a metal−organic framework: boosting electron−hole separation via electron trap states. *J. Am. Chem. Soc.* **2015**, *137*, 13440−13443.

(18) Liu, J.; Fan, Y.-Z.; Li, X.; Wei, Z.; Xu, Y.-W.; Zhang, L.; Su, C.-Y. A porous rhodium (III)-porphyrin metal-organic framework as an efficient and selective photocatalyst for CO_2 reduction. *Appl. Catal., B* **2018**, *231*, 173−181.

(19) Chen, E. X.; Qiu, M.; Zhang, Y. F.; Zhu, Y. S.; Liu, L. Y.; Sun, Y. Y.; Bu, X.; Zhang, J.; Lin, Q. Acid and Base Resistant Zirconium Polyphenolate-Metalloporphyrin Scaffolds for Efficient CO_2 Photoreduction. *Adv. Mater.* **2018**, *30*, No. 1704388.

(20) Gooch, A.; Sizochenko, N.; Rasulev, B.; Gorb, L.; Leszczynski, J. In vivo toxicity of nitroaromatics: A comprehensive quantitative structure−activity relationship study. *Environ. Toxicol. Chem.* **2017**, *36*, 2227−2233.

(21) (a) Rabbani, M.; Heidari-Golafzani, M.; Rahimi, R. Synthesis of $TCPP/ZnFe_2O_4@$ ZnO nanohollow sphere composite for degradation of methylene blue and 4-nitrophenol under visible light. *Mater. Chem. Phys.* **2016**, *179*, 35−41. (b) Rabbani, M.; Bathaee, H.; Rahimi, R.; Maleki, A. Photocatalytic degradation of p-nitrophenol and methylene blue using Zn-TCPP/Ag doped mesoporous TiO_2 under UV and visible light irradiation. *Desalin. Water Treat.* **2016**, *57*, 25848−25856.

(22) Gao, W.-Y.; Wojtas, L.; Ma, S. A porous metal−metalloporphyrin framework featuring high-density active sites for chemical fixation of CO_2 under ambient conditions. *Chem. Commun.* **2014**, *50*, 5316−5318.

(23) Wang, X.-S.; Chrzanowski, M.; Kim, C.; Gao, W.-Y.; Wojtas, L.; Chen, Y.-S.; Zhang, X. P.; Ma, S. Quest for highly porous metal−metalloporphyrin framework based upon a custom-designed octatopic porphyrin ligand. *Chem. Commun.* **2012**, *48*, 7173−7175.

(24) Akbarzadeh, A.; Nekoeifard, M.; Rahmatollah, R.; Keshavarz, M. Two spectral QSPR models of porphyrin macromolecules for chelating heavy metals and different ligands released from industrial solvents: CH_2Cl_2, $CHCl_3$ and toluene. *SAR QSAR Environ. Res.* **2020**, *31*, 347−371.

(25) (a) Rahimi, R.; Keshavarz, M. H.; Akbarzadeh, A. R. Prediction of the Density of Energetic Materials on the Basis of their Molecular Structures. *Cent. Eur. J. Energ. Mater.* **2016**, *13*, 73−101. (b) Keshavarz, M.; Akbarzadeh, A. A simple approach for assessment of toxicity of nitroaromatic compounds without using complex

descriptors and computer codes. *SAR QSAR Environ. Res.* **2019**, *30*, 347−361.

(26) (a) Keshavarz, M. H.; Akbarzadeh, A. R.; Rahimi, R.; Jafari, M.; Pasandideh, M.; Sadeghi, R. A reliable method for prediction of enthalpy of fusion in energetic materials using their molecular structures. *Fluid Phase Equilib.* **2016**, *427*, 46−55. (b) Keshavarz, M. H.; Rahimi, R.; Akbarzadeh, A. R. Two novel correlations for assessment of crystal density of hazardous ionic molecular energetic materials using their molecular structures. *Fluid Phase Equilib.* **2015**, *402*, 1−8. (c) Najafi, M.; Akbarzadeh, A. R.; Rahimi, R.; Keshavarz, M. H. QSPR model for estimation of photodegradation average rate of the porphyrin-TiO_2 complexes and prediction of their biodegradation activity and toxicity: Engineering of two annihilators for water/waste contaminants. *J. Mol. Struct.* **2022**, *1249*, No. 131463.

(27) Sadeghi, N.; Sharifnia, S.; Arabi, M. S. A porphyrin-based metal organic framework for high rate photoreduction of CO_2 to CH_4 in gas phase. *J. CO_2 Util.* **2016**, *16*, 450−457.

(28) Wang, L.; Jin, P.; Huang, J.; She, H.; Wang, Q. Integration of copper (II)-porphyrin zirconium metal−organic framework and titanium dioxide to construct Z-scheme system for highly improved photocatalytic CO_2 reduction. *ACS Sustainable Chem. Eng.* **2019**, *7*, 15660−15670.

(29) Jin, J. Porphyrin-based metal−organic framework catalysts for photoreduction of CO_2: understanding the effect of node connectivity and linker metalation on activity. *New J. Chem.* **2020**, *44*, 15362−15368.

(30) (a) Rahimi, R.; Keshavarz, M. H.; Akbarzadeh, A. R. Prediction of the Density of Energetic Materials on the Basis of their Molecular Structures. *Cent. Eur. J. Energ. Mater.* **2016**, *13*, 73−101. (b) Moharramnejad, M.; Tayebi, L.; Akbarzadeh, A. R.; Maleki, A. A simple, robust, and efficient structural model to predict thermal stability of zinc metal-organic frameworks (Zn-MOFs): The QSPR approach. *Microporous Mesoporous Mater.* **2022**, *336*, 111815.

(31) (a) Rücker, C.; Rücker, G.; Meringer, M. y-Randomization and its variants in QSPR/QSAR. *J. Chem. Inf. Model.* **2007**, *47*, 2345−2357. (b) Daoui, O.; Mazoir, N.; Bakhouch, M.; Salah, M.; Benharref, A.; Gonzalez-Coloma, A.; Elkhattabi, S.; Yazidi, M. E.; Chtita, S. 3D-QSAR, ADME-Tox, and molecular docking of semisynthetic triterpene derivatives as antibacterial and insecticide agents. *Struct. Chem.* **2022**, *33*, 1063−1084.

(32) Zhuang, B.; Xiangqing, L.; Ge, R.; Kang, S.; Qin, L.; Li, G. Assembly and electron transfer mechanisms on visible light responsive 5, 10, 15, 20-meso-tetra (4-carboxyphenyl) porphyrin/cuprous oxide composite for photocatalytic hydrogen production. *Appl. Catal., A* **2017**, *533*, 81−89.

(33) (a) Xiao, J.-D.; Jiang, H.-L. Metal−organic frameworks for photocatalysis and photothermal catalysis. *Acc. Chem. Res.* **2019**, *52*, 356−366. (b) Kumar, B.; Llorente, M.; Froehlich, J.; Dang, T.; Sathrum, A.; Kubiak, C. P. Photochemical and photoelectrochemical reduction of CO_2. *Annu. Rev. Phys. Chem.* **2012**, *63*, 541−569.